J. Fluid Mech. (2011), *vol.* 689, *pp.* 417–433. © Cambridge University Press 2011
doi:10.1017/jfm.2011.422

Flow instabilities between two parallel planes semi-obstructed by an easily penetrable porous medium

N. Silin[1], J. Converti[1], D. Dalponte[2] and A. Clausse[2]†

[1] CONICET-CNEA and Instituto Balseiro, 8400 Bariloche, Argentina

[2] CNEA-CONICET and Universidad Nacional del Centro, 7000 Tandil, Argentina

(Received 1 November 2010; revised 27 June 2011; accepted 23 September 2011; first published online 17 November 2011)

A study of instabilities in planar flows produced by the presence of a parallel penetrable porous obstruction is presented. The case considered is a flow between parallel plates partially obstructed by a porous medium. The most unstable perturbation modes are obtained solving numerically the eigenvalue problem derived from the linear stability analysis of the two-dimensional Navier–Stokes equations applied to the geometry of interest. The analysis leads to an extended Orr–Sommerfeld equation including a porous term. It was found that the ratios of the permeability and depth of the obstruction with respect to the free flow layer depth are the relevant parameters influencing the stability margin and the structure of the most unstable modes. To validate the conclusions of the theoretical analysis, an experiment with air flowing through a channel semi-obstructed by a regular array of cylindrical wires was performed. The critical Reynolds number, which was determined by measuring the amplitude of velocity fluctuations at the interface of the porous medium, agrees with the theoretical predictions. The dominant instability mode was characterized by the cross-section profile of the root mean square of the velocity perturbations, which matches reasonable well with the eigenfunction of the most unstable eigenvalue. Also, the wavenumber was determined by correlating the velocity measurements in two sequential locations along the channel, which compares well with the theoretical value.

Key words: boundary layer structure, instability, low-Reynolds-number flows

1. Introduction

The study of flows in geometries that include complex obstructions is of interest in various branches of engineering. A special case that finds applications in heat transfer and environmental engineering is the parallel flow over easily penetrable porous media. This occurs for example when wind blows over vegetation or trees (Poggi & Katul 2008), water channels with aquatic plants (López & García 2001) and rivers flooding over plains with vegetation (Gayev & Hunt 2007) or wind over cities (Ghisalberti 2009). Analogous flows also appear in technological applications such as cooling flows over electronic components, cooler fins and metallic sponges, which can be regarded as porous walls (Breugem, Boersma & Uittenbogaard 2006).

† Email address for correspondence: clausse@exa.unicen.edu.ar

https://doi.org/10.1017/jfm.2011.422 Published online by Cambridge University Press

In this kind of flow, the velocity profile generally shows a point of inflexion about the frontier between the regions of obstructed and free flow (Beavers & Joseph 1967), similar to what happens in a plane mixing layer (Raupach, Finnigan & Brunet 1996; White & Nepf 2007). This feature brings about two-dimensional instabilities that result in large-scale coherent structures, which in turn enhance the transversal diffusion both in the porous medium as well as in the free flow near the interface (Raupach *et al.* 1996). For this reason, such structures can affect the concentration of scalars and the velocity profile, not only in the neighbourhood of the interface but also up to a significant distance apart (Finnigan 2000; Breugem *et al.* 2006).

Inflexion points, instabilities and periodic structures may also be seen in compound channels (Bousmar *et al.* 2005; Ghisalberti 2009), which are assemblies of two or more regions with different hydraulic behaviour. Examples of this kind of channel are flows parallel to slots or fins, flood plains, parallel rod bundles, etc. Research on compound channels reports large-scale quasiperiodic hydrodynamic structures similar to those found in flows parallel to porous media. A comprehensive review on compound channels and flows parallel to rod bundles can be found in Meyer (2010). Recently, Merzari *et al.* (2008) performed linear stability studies about two kinds of compound channels: annular eccentric and two rectangular channels joined through a gap. A notable result is the presence of an asymmetrical pressure wave that resembles the large-scale cellular structures measured in controlled experiments (Lexmond, Mudde & Van der hagen 2005).

In the present work, a flow in a channel partially obstructed by a very high-porosity and high-permeability porous medium is studied. This kind of flow allows a two-dimensional theoretical treatment while retaining the main physics of real flows in slender rectangular channels with a partial easily penetrable porous obstruction. The present work contains a linear stability analysis similar to those performed by Socolofsky & Jirka (2004) for flat mixing interfaces and White & Nepf (2007) for shallow flows parallel to porous media, but focusing on a porous medium that complies with Darcy's law. Hill & Straughan (2008) numerically investigated the stability of a similar problem consisting of a flow overlying a porous medium saturated with the same fluid. A three-layer configuration was adopted, namely a Newtonian fluid overlying a Brinkman porous transition layer, which in turn overlies a Darcy-type porous substratum. They found that there are two modes of instability corresponding to the fluid and to the porous layer. The present analysis considers a simpler model which is able to describe a wider parameter space, being complementary with the results of Hill & Straughan. To validate the present analysis, a set of experimental data measured on a slender channel with a rectangular cross-section obstructed by a regular array of wires is compared with the theoretical model.

2. Model of easily penetrable porous media

The behaviour of easily penetrable porous media can be produced by a variety of natural or artificial objects that offer resistance to the free flow. The flow resistance characteristics depend on the geometry, flow–structure interaction and characteristic dimensions of the porous layer. The present work deals with porous media obeying Darcy's law, where the resistance is proportional to the dynamic viscosity μ and the flow velocity $\boldsymbol{u}$.

Let us consider a flow bounded by two parallel flat plates where part of the cross-section is obstructed by an easily penetrable porous medium as shown in figure 1. The origin is located on the edge of the porous medium. The porous medium will be

https://doi.org/10.1017/jfm.2011.422 Published online by Cambridge University Press

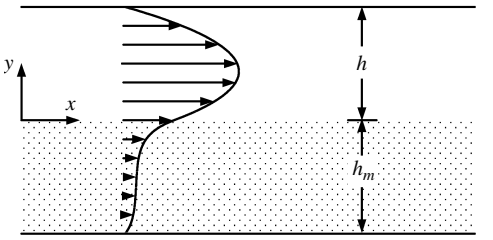


FIGURE 1. Diagram of the system under study. The lower half of the channel is occupied by a porous media and the upper half is free.

characterized by a volumetric resistance in the opposite direction to the velocity field $\boldsymbol{u}$ given by the Darcy law:

$$\boldsymbol{D} = -\frac{\mu\,\boldsymbol{u}}{\kappa} \tag{2.1}$$

where μ is the dynamic viscosity and κ is the permeability of the porous medium. In our case we consider only porous media that are homogeneous and isotropic, therefore κ is a constant scalar. Assuming incompressible flow, the continuity and Navier–Stokes equations in such a flow are

$$\boldsymbol{\nabla}\cdot\boldsymbol{u} = 0 \tag{2.2}$$

$$\frac{\partial \boldsymbol{u}}{\partial t} + \boldsymbol{u}\cdot\boldsymbol{\nabla}\boldsymbol{u} = -\frac{1}{\rho}\boldsymbol{\nabla}p - \frac{\upsilon}{\kappa}H(y)\,\boldsymbol{u} + \upsilon\nabla^2\boldsymbol{u}, \tag{2.3}$$

where p is the pressure field, υ is the kinematic viscosity and $H(y)$ is the Heaviside function, whose value is 1 in the porous region and 0 in the free flow. For the porous region (2.3) in steady state is similar to the Brinkman model considering the same viscosity for free and porous layers and a porous medium with zero volume fraction. These assumptions are appropriate for easily penetrable porous media. A more detailed model including independent viscosities and porosity as parameters can be found in Hill & Straughan (2008).

2.1. *Steady state*

Assuming steady-state fully developed parallel flow in two Cartesian dimensions, i.e. $\partial\boldsymbol{u}/\partial t = 0$, $\boldsymbol{u} = (U, 0)^{\mathrm{T}}$ and $\boldsymbol{\nabla}p = (\mathrm{d}p/\mathrm{d}x, 0)^{\mathrm{T}}$, (2.2)–(2.3) reduce to

$$U'' - \frac{1}{\kappa}H(y)U = \frac{1}{\mu}\frac{\mathrm{d}p}{\mathrm{d}x}, \tag{2.4}$$

where the prime denotes derivative with respect to y. The boundary conditions are

$$U = 0 \quad \text{at } y = -h_m \text{ and } y = h. \tag{2.5}$$

The solution of (2.4) with those boundary conditions is

$$\frac{U}{U_o} = \frac{8}{\sigma^2} + \left(\tilde{U}_B - \frac{8}{\sigma^2}\right)\cosh\frac{\sigma y}{h} + \left[\frac{8}{\sigma^2} + \left(\tilde{U}_B - \frac{8}{\sigma^2}\right)\cosh(\beta\sigma)\right]\frac{\sinh\dfrac{\sigma y}{h}}{\sinh(\beta\sigma)}; \quad -h_m < y < 0 \tag{2.6a}$$

$$\frac{U}{U_o} = \left(\tilde{U}_B + 4\frac{y}{h}\right)\left(1 - \frac{y}{h}\right); \quad 0 < y < h \tag{2.6b}$$

https://doi.org/10.1017/jfm.2011.422 Published online by Cambridge University Press

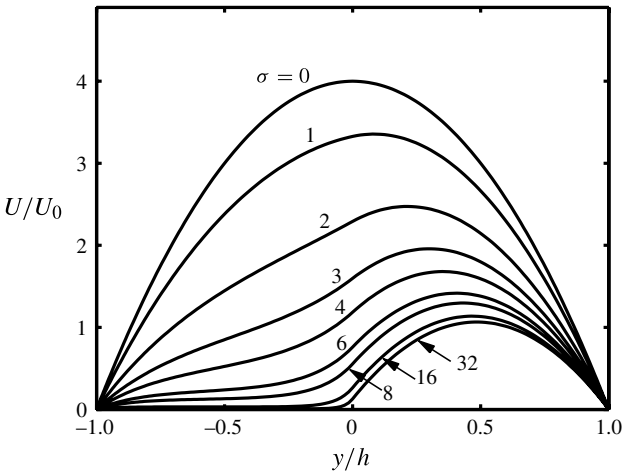


FIGURE 2. Analytical steady-state velocity profiles for different porous resistivities $\sigma\,(\beta = 1)$.

where U_o is a characteristic velocity given by

$$U_o = -\frac{h^2}{8\mu}\frac{\mathrm{d}p}{\mathrm{d}x}, \tag{2.7}$$

σ is a dimensionless resistivity characterizing the porous media, given by

$$\sigma = \frac{h}{\sqrt{\kappa}}, \tag{2.8}$$

β is the porous to free-layer depth ratio,

$$\beta = \frac{h_m}{h}, \tag{2.9}$$

and

$$\tilde{U}_B = \frac{4\sinh(\beta\sigma) + \dfrac{8}{\sigma}(\cosh(\beta\sigma) - 1)}{\sinh(\beta\sigma) + \sigma\cosh(\beta\sigma)} \tag{2.10}$$

is the ratio between the velocity at $y = 0$ and U_o, which is determined by imposing tangential stress continuity. This condition is chosen here for its simplicity and considering the fact that we focus on easily penetrable porous media. More sophisticated boundary conditions on the tangential stress at the porous interface have also been proposed in order to obtain the desired accuracy when assessing a flow over a given porous material (Larson & Higdon 1986; Hill & Straughan 2008).

Figure 2 shows different velocity profiles obtained by varying the parameter σ for a porous-to-free-layer depth ratio $\beta = 1$. It can be seen that, as σ increases, the velocity in the porous region decreases relative to the free-flow region. Except for relatively small values of σ, the velocity profile presents an inflexion point close to the porous layer interface. As the resistivity of the porous medium increases, the velocity profile tends asymptotically to a Poiseuille flow in a free channel of width h. Similarly, as σ tends to zero the velocity profile tends asymptotically to a Poiseuille flow in a channel of width $2h$.

https://doi.org/10.1017/jfm.2011.422 Published online by Cambridge University Press

2.2. *Stability analysis*

Let us partition the motion into a mean flow $U(y)$ and a small perturbation superimposed on it, that is

$$\boldsymbol{u} = (U + u, v)^{\mathrm{T}}. \tag{2.11}$$

Then, (2.2) and (2.3) are written to first order as

$$\frac{\partial u}{\partial x} + \frac{\partial v}{\partial y} = 0 \tag{2.12a}$$

$$\frac{\partial u}{\partial t} + U\frac{\partial u}{\partial x} + v\frac{\partial U}{\partial y} = -\frac{1}{\rho}\frac{\partial p}{\partial x} - \frac{\upsilon}{\kappa}H(y)u + \upsilon\left(\frac{\partial^2 u}{\partial x^2} + \frac{\partial^2 u}{\partial y^2}\right) \tag{2.12b}$$

$$\frac{\partial v}{\partial t} + U\frac{\partial v}{\partial x} = -\frac{1}{\rho}\frac{\partial p}{\partial y} - \frac{\upsilon}{\kappa}H(y)v + \upsilon\left(\frac{\partial^2 v}{\partial x^2} + \frac{\partial^2 v}{\partial y^2}\right). \tag{2.12c}$$

Let us assume now typical harmonic perturbations:

$$u = \phi'(y)\mathrm{e}^{\mathrm{i}(kx-\omega t)} \tag{2.13}$$

$$v = \mathrm{i}k\phi(y)\mathrm{e}^{\mathrm{i}(kx-\omega t)} \tag{2.14}$$

$$p = \varphi(y)\mathrm{e}^{\mathrm{i}(kx-\omega t)} \tag{2.15}$$

which ensure that (2.12*a*) is satisfied. Combining (2.12)–(2.15) leads to

$$(c-U)\phi' + U'\phi = \frac{\varphi}{\rho} + \frac{\upsilon}{\mathrm{i}k\kappa}H(y)\phi' - \frac{\upsilon}{\mathrm{i}k}(\phi''' - k^2\phi') \tag{2.16a}$$

$$k^2(U-c)\phi = -\frac{\varphi'}{\rho} - \frac{\upsilon k}{\mathrm{i}\kappa}H(y)\phi' - \frac{\upsilon k}{\mathrm{i}}(k^2\phi + \phi'') \tag{2.16b}$$

where $c = \omega/k$ is a complex parameter whose real part is the propagation velocity of the perturbation, and its imaginary part determines the amplification or attenuation of the perturbation depending on the sign.

Eliminating φ from (2.16) the following extended Orr–Sommerfeld equation, with an additional term for linear friction, can be obtained:

$$\begin{aligned}(c-U)\phi'' + [U'' + k^2(U-c)]\phi = {} & \frac{\upsilon}{\mathrm{i}k\kappa}[H(y)(\phi'' - k^2\phi) + H'(y)\phi'] \\ & + \frac{\upsilon}{\mathrm{i}k}(-\phi'''' + 2k^2\phi'' - k^4\phi).\end{aligned} \tag{2.17}$$

Since u and v vanish at the channel walls, the corresponding boundary conditions are

$$\phi(h) = \phi'(h) = \phi(-h_m) = \phi(-h_m) = 0. \tag{2.18}$$

White & Nepf (2007) obtained an expression analogous to (2.17) for a quadratic dependence of the distributed friction with the velocity. The solution of (2.17) is equivalent to finding the eigenvalues c_i and the corresponding eigenfunctions or modes ϕ_i. The stability threshold is defined by the critical values of the parameters σ, k and $Re_h = hU_o/\upsilon$, for which the largest imaginary part of c vanishes (Schlichting & Gersten 2000).

Equation (2.17) was numerically solved using the Matlab Differentiation Matrix Suite (Weideman & Reddy 2000), based on the spectral collocation method with Chebyshev interpolants. Figure 3 show the critical stability curves in the plane (k, Re_h) for different resistivities σ and a porous-to-free-layer depth ratio $\beta = 1$. It is worth noting that the two extreme values of σ (i.e. $\sigma = 0$ and $\sigma = \infty$) correspond to

https://doi.org/10.1017/jfm.2011.422 Published online by Cambridge University Press

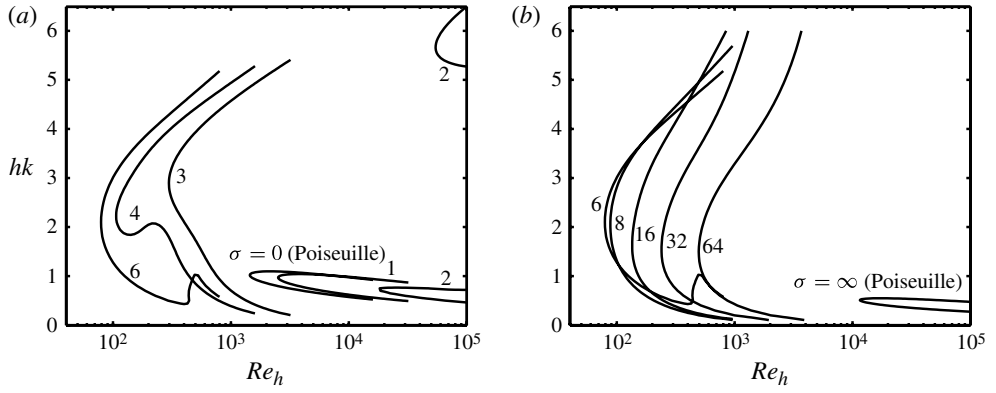


FIGURE 3. Stability curves for different values of porous resistivity σ. For clarity, curves for σ between 0 and 6 are shown in (a) and curves for σ between 6 and ∞ are shown in (b). The flow is stable on the concave side of each curve.

Poiseuille flows. For $\sigma = 0$, the Poiseuille flow covers the whole channel width from $-h_m$ to h, and the classical result in which the flow destabilizes at $Re_h \sim 1500$ with wavenumber $k \sim h^{-1}$ is obtained. Note in figure 2 that the channel width is $2h$ and the mean velocity is $2U_o$. For $\sigma = \infty$, a Poiseuille flow in a channel of width h and a mean velocity $U_o/2$ is obtained.

Interestingly, when semi-obstructing the channel with a very permeable porous media ($\sigma = 1$) the flow becomes more stable, i.e. the critical Reynolds number increases. For the case of $\sigma = 2$, there are two unstable zones or lobes. For lower wavenumbers the instability mode is similar to the Poiseuille instability. In turn, the mode at higher values of k responds to a different instability mechanism that localizes at the porous layer boundary: a shear layer instability mode. For larger values of σ the two lobes merge; we propose to call this regime the porous instability mode, covering a broader range of wavelengths and showing decreasing critical Reynolds numbers. The critical stability curve for $\sigma = 4$ presents a curl around $Re_h = 100$, which is a footprint left by the clash between both instability modes. This curl also appears in the curve of $\sigma = 6$. A curl in the stability curve has also been found for certain conditions by Hill & Straughan (2008). For $\sigma > 6$ the critical Reynolds number begins to increase again (figure 3b).

Figure 4 shows the dependence of the critical Re_h and k on σ for $\beta = 1$. For $\sigma < 2.1$, the presence of the porous media stabilizes the flow by increasing the critical Re_h, mostly due to the friction added by the media. From $\sigma = 2.1$ a second instability mode prevails, which becomes more unstable as σ increases (i.e. the critical Re_h decreases). The transition between modes is evidenced by the discontinuity of the most dangerous wavenumber k at $\sigma = 2.1$, which jumps from $0.75h^{-1}$ to $5.7h^{-1}$. Note in figure 4 that, as σ increases beyond 2.1, the critical Re_h reaches the minimum value 79 at $\sigma = 6$, with $k = 2.1h^{-1}$. Further increases of σ progressively stabilize the flow approaching asymptotically the Poiseuielle flow in a channel of width h.

Figure 5(a) shows the module of the most unstable eigenfunctions for $\sigma = 1$ at the critical $Re_h = 2520$. The profiles of u and v are similar to those found in the Poiseuille flow, with a u minimum and a v maximum around the channel centre line, slightly skewed towards the free flow side. Figures 5(b) and 5(c) show the eigenfunctions modules of the most unstable perturbation mode for $\sigma = 2$, corresponding to the

https://doi.org/10.1017/jfm.2011.422 Published online by Cambridge University Press

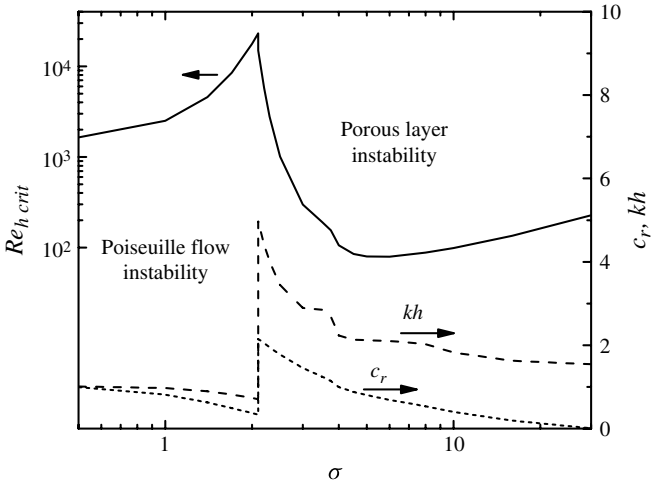


FIGURE 4. Variation of the critical parameters (i.e. the most unstable mode) with the resistivity σ of the porous semi-obstruction. For $\sigma < 1.7$ the obstruction stabilizes the flow. For $\sigma < 1.7$ a second instability mode prevails with higher wavenumber k and wave velocity $c_r = Re(c)/U_o$. The most unstable case occurs at $\sigma = 6$.

lower and upper wavenumber lobes, respectively (see figure 3). It can be seen that the eigenfunctions corresponding to the lower wavenumber (figure 5*b*) still resemble the instabilities of the Poiseuille flow with u showing two characteristic peaks near the walls, whereas the eigenfunctions of the upper wavenumber (figure 5*c*) show a completely different behaviour with higher values at the channel centre line. The physical interpretation is that the lower lobe corresponds to instabilities generated at the wall, while the higher lobe is related to shear layer instabilities at the porous media interface. For larger σ, the module of the eigenfunctions of the most unstable perturbation mode are shown in figures 5(*d*) and 5(*e*). It can be seen that as σ increases the fluctuations in the porous region are progressively damped. This trend continues until the Poiseuille condition for half of the channel is reached asymptotically as σ tends to ∞ (figure 5*f*).

The stability curves for different porous-to-free-layer depth ratios were calculated for three values of σ, namely $\sigma = 3$, 6 and 128. Figure 6 shows the stability margins for $\sigma = 3$ and different values of β. It can be seen that the critical Re_h is very sensitive to the depth of the porous layer, with a mode transition for $\beta \cong 0.38$. For $\sigma = 6$ the stability margins are shown in figure 7, presenting a monotonous variation between $\beta = 1$ and $\beta = 0$, which corresponds to the Poiseuille flow. Figure 8 shows the stability margins for $\sigma = 128$, which represents a porous medium with low permeability. As in the other cases, the flow becomes more stable as β is decreased. Interestingly, in this case, for $\beta < 0.075$ the critical Re_h becomes larger than that corresponding to the Poiseuille flow occupying the free flow layer between 0 and h (i.e. $\sigma = \infty$ in figure 3*b*); that is, there is a stabilizing effect. Also, note that for $\beta = 0.15$ and $\beta = 0.1$ two upper lobes appears corresponding to a porous instability mode; but this mode does not become predominant for the studied range of conditions.

White & Nepf (2007) suggested that the shear instability is largely determined by the free layer properties, such as length scale and velocity, whereas the influence of the porous layer penetration length is relatively unimportant. In the present case, the

https://doi.org/10.1017/jfm.2011.422 Published online by Cambridge University Press

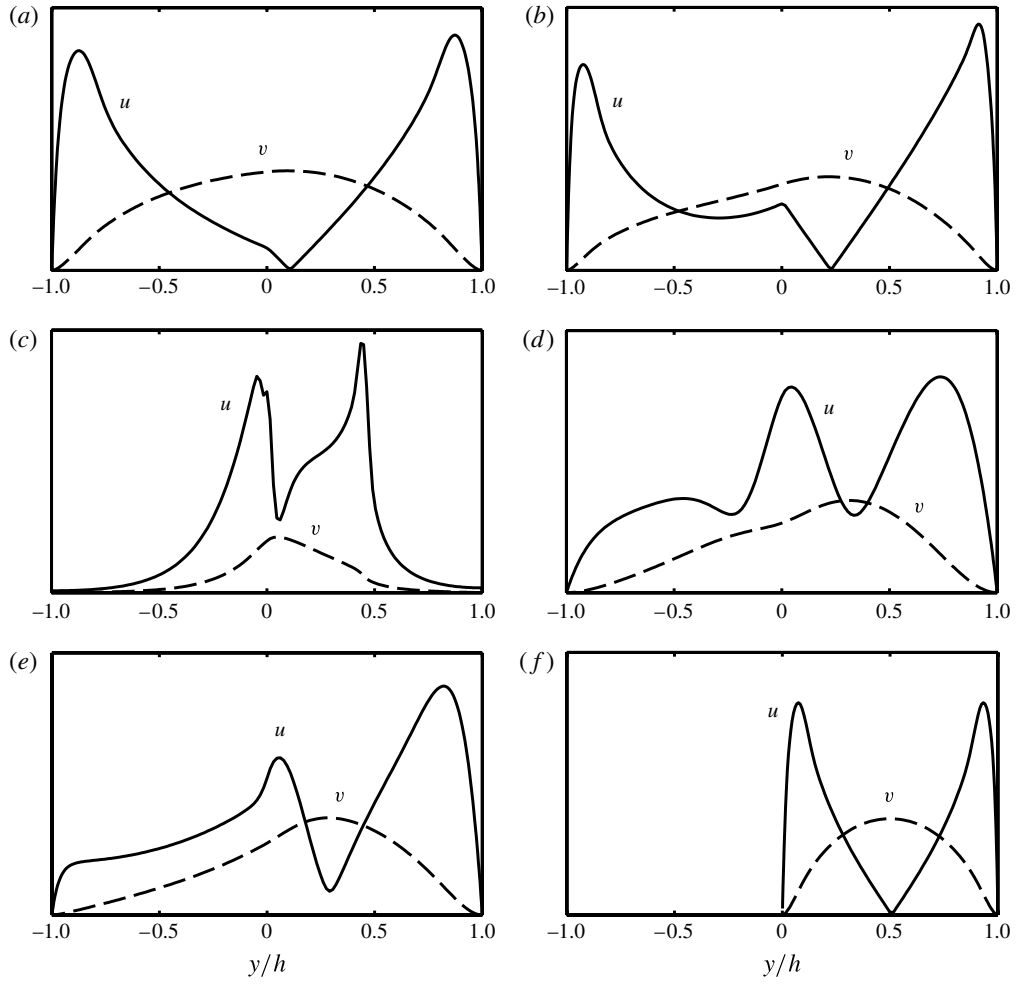


FIGURE 5. Eigenfunctions of the perturbations for different porous conductivities. The values of Re_h and k correspond to the most unstable mode: (*a*) $\sigma = 1$, $Re_h = 2520$, $kh = 0.97$; (*b*) $\sigma = 2$, $Re_h = 18\,300$, $kh = 0.74$; (*c*) $\sigma = 2$, $Re_h = 54\,500$, $kh = 5.65$; (*d*) $\sigma = 6$, $Re_h = 80$, $kh = 2.10$; (*e*) $\sigma = 32$, $Re_h = 239$, $kh = 1.50$; (*f*) $\sigma = \infty$, $Re_h = 11\,560$, $kh = 0.51$.

latter is only observed for cases with high values of σ and β. In turn, for low values of σ and β, the porous layer penetration length becomes important.

3. Comparison with experimental measurements

The stability analysis was compared with experimental data from the flow in a rectangular channel semi-obstructed by a regular array of cylindrical wires (figure 9). Air from the room was induced to pass through the test section by a fan located at the outlet of the device. At the entrance, the flow was preconditioned by a honeycomb and a screen straightener, and a second curved screen produced an inlet parabolic velocity distribution. The wires were 0.25 mm in diameter and spaced every 5 mm in the flow direction (x-axis) and 2.5 mm in the transverse direction (y-axis). This arrangement

https://doi.org/10.1017/jfm.2011.422 Published online by Cambridge University Press

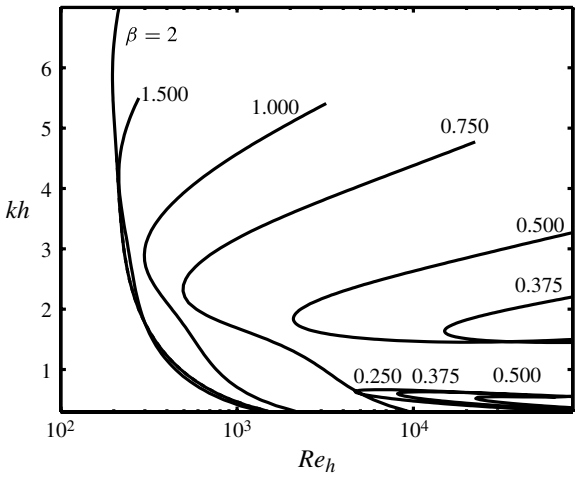


FIGURE 6. Stability curves for porous resistivity $\sigma = 3$ and different porous-to-free-layer depth ratios β.

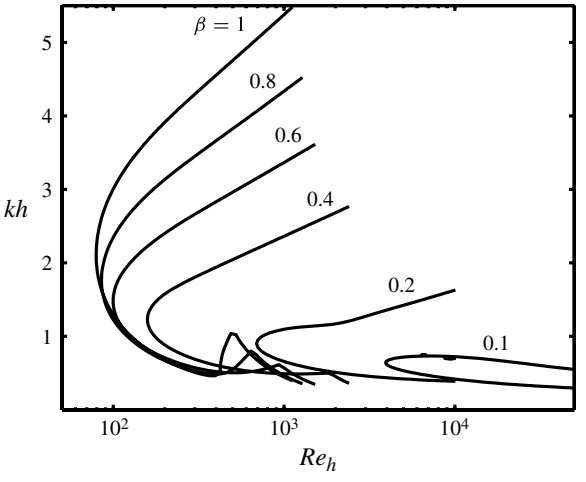


FIGURE 7. Stability curves for porous resistivity $\sigma = 6$ and different porous-to-free-layer depth ratios β.

recreated the most unstable situation occurring for $\sigma \sim 6$ (see figure 4), while the porous region can still be considered homogeneous. The gap between wires in the flow direction was sufficient to transverse the probe through the porous region. The total size of the test section was 57 mm × 100 mm × 920 mm, which provides a satisfactory spatial resolution of the probes.

The application of a porous medium model to a complex obstruction implies a spatial and temporal averaging process as discussed, for example, by Larson & Higdon (1986). For a porous model to be valid, the spatial averaging scales should be smaller than the scales of the flow features represented by the model. In the present experiment two characteristic scales should be considered: the minimum instability wavelength and the viscous diffusion scale of the wire wakes. In figure 4 it can be

https://doi.org/10.1017/jfm.2011.422 Published online by Cambridge University Press

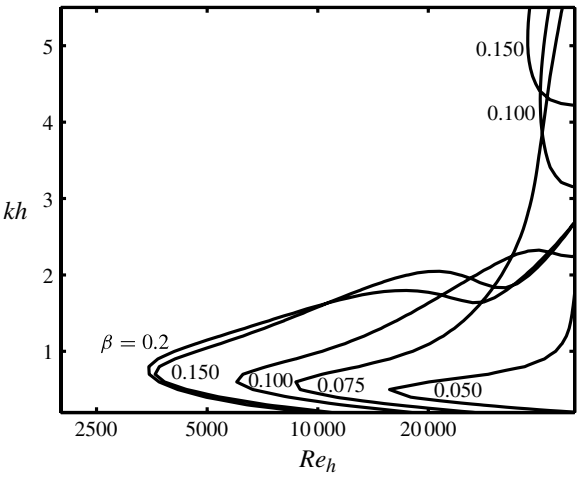


FIGURE 8. Stability curves for porous resistivity $\sigma = 128$ and different porous-to-free-layer depth ratios β.

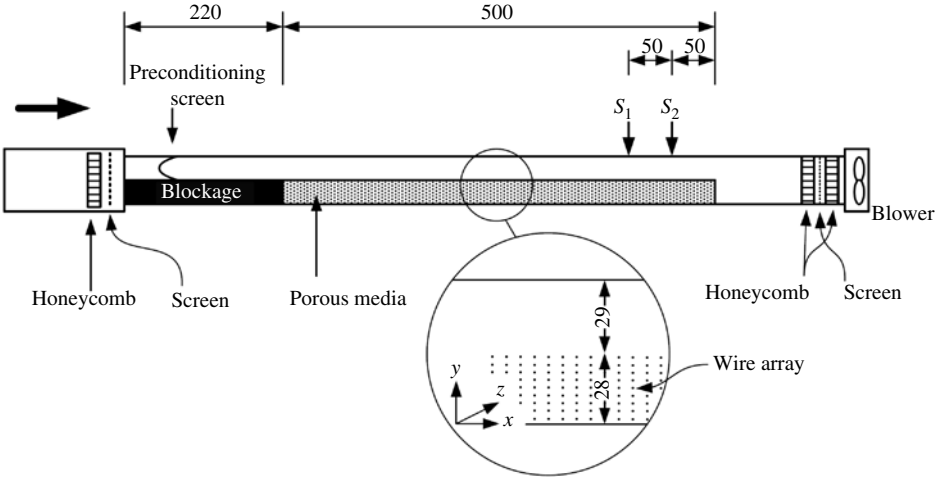


FIGURE 9. Schematics of the experimental test section.

seen that maximum critical wavenumber is approximately $5h^{-1}$. The corresponding minimum expected wavelength is 36 mm, which is much longer than the streamwise separation of the wires. On the other hand, the viscous diffusion thickness normal to the main flow direction, x, can be estimated as (Mathieu & Scott 2000)

$$\delta \approx \left(\frac{\nu}{U_l}\right)^{1/2} x^{1/2}, \tag{3.1}$$

where U_l is the local volume average velocity. Taking x as the wire spacing in the flow direction and U_l the maximum velocity at the porous medium interface, gives $\delta \approx 1.3$ mm. This upper bound is half the transversal wire separation, indicating that the set-up is appropriate to represent a homogeneous porous medium.

https://doi.org/10.1017/jfm.2011.422 Published online by Cambridge University Press

The applicability of Darcy's law is limited to low values of the local Reynolds number of the porous medium elements, that is (Larson & Higdon 1986):

$$Re_d = \frac{U_l d}{\nu}, \tag{3.2}$$

where d is the porous element characteristic diameter. The maximum value of Re_d for a homogeneous porous medium occurs at the porous layer interface, where the following relation holds:

$$U_l = U_0 \tilde{U}_B. \tag{3.3}$$

Therefore, to ensure $Re_d < O(1)$, the global Reynolds number Re_h should satisfy

$$Re_d^{MAX} = Re_h \tilde{U}_B \frac{\mathrm{d}}{h} < O(1). \tag{3.4}$$

Equation (3.4) is satisfied for the present experimental conditions ($Re_d < 0.7$).

A hot-wire anemometer was used to map the channel velocity field. Since at the working conditions the contribution of natural convection from the hot wire itself is not negligible, the hot-wire diameter, overheating and orientation had to be carefully considered (Bruun 1995). The highest sensitivity is granted when both forced and natural convection contributions add up in the same direction. Accordingly, the test section was placed vertically with air flow forced upwards. Preliminary measurements were performed with hot-wire diameters of 2 and 15 μm. The latter was finally selected as it provides higher sensitivity while the spatial and time resolutions are satisfactory for the present study. The working overheat temperature was 230 K.

Two hot-wire configurations where used. For the laminar mean velocity profile, i.e. measurements at $Re = 63$, the hot wire was aligned with the z-axis and traversed in the y-direction. This allows for higher spatial resolution in the y-axis. For the flow presenting x and y velocity component fluctuations, the hot wire was aligned with the y-axis. This configuration is less sensitive to y velocity components, so the x component of the velocity and velocity fluctuations could be measured.

The anemometer was calibrated using a device consisting of an upper water tank, a flow control valve, an intermediate tank where air is displaced by the water, and a tube 10.0 mm ID and 1 m long to obtain a developed laminar flow (Yue & Malmstrom 1998). The volumetric flow of air was calculated by measuring the filling time of the intermediate tank. The velocity at the tube outlet is calculated assuming a parabolic radial profile. The lower detection bound of the anemometer is 5×10^{-3} m s^{-1}, although smaller velocity fluctuations can be measured.

In order to assess systematic errors, the channel was first profiled with zero net flow. A slight asymmetry was detected close to the walls, which is attributed to heat transfer enhancement by the walls (Chew, Khoo & Li 1998). Another source of error was introduced by the intrusion of the hot wire itself, which generates different natural convection in the porous and free flow layers. Both effects were accounted for to correct the measurements and to calculate the velocity and Re_h error bands.

The x component of the velocity was profiled at position S_1 (see figure 9) for different inlet flow rates. At each transversal location the output signal of the anemometer was recorded during 60 s with 1 kHz sampling rate. Figure 10 shows the parallel velocity profile at position S_1 for $Re_h = 65$ (stable) and $Re_h = 100$ (marginally unstable). The curves shown in figure 10 are the best fit of (2.6) and (2.10), which corresponds to $\sigma = 6$. This value is used in what follows to compare the theoretical predictions with the experimental results.

https://doi.org/10.1017/jfm.2011.422 Published online by Cambridge University Press

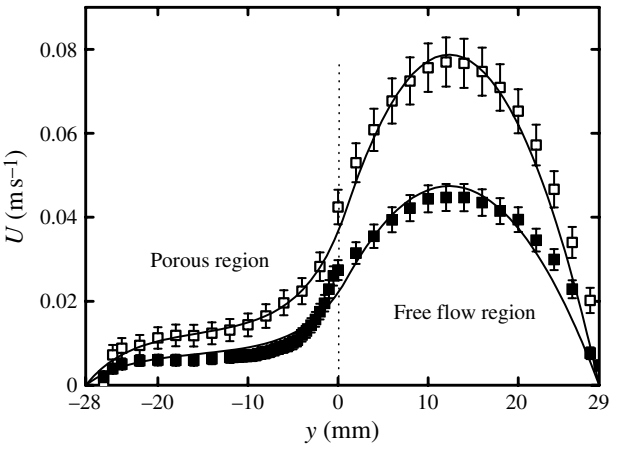


FIGURE 10. Profile of the mean parallel velocity at position S_1 with (•) $Re_h = 65$ and (○) $Re_h = 100$. The left half is occupied by the porous media. The curves correspond to the theoretical results obtained by (2.6) and (2.10) with $\sigma = 6$.

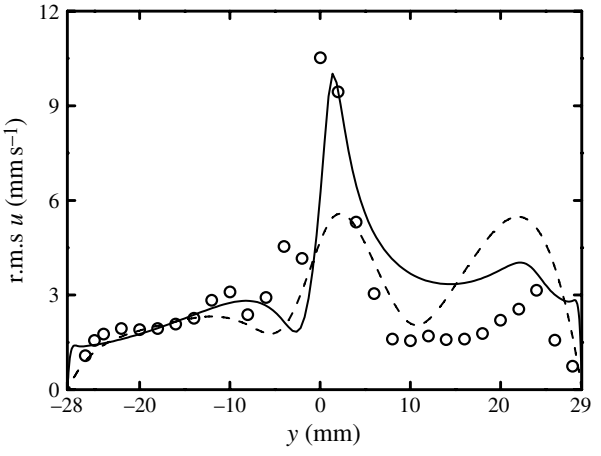


FIGURE 11. Profile of the r.m.s. of the parallel velocity perturbation measured at axial position S_1 with $Re_h = 100$. The curves are the module of the eigenfunction of the perturbation u for $\sigma = 6$, $Re_h = 100$ (dashed) and $Re_h = 10\,000$ (solid).

In figure 10 a slight difference can be observed between the calculated and the experimental results for $Re_h = 65$ (stable) around the porous layer interface. It is also possible to observe a change in the velocity gradient at this point, which can be attributed to the limitation of Darcy's law to capture the behaviour of the flow in the outmost row of wires (Larson & Higdon 1987). This raises questions of whether the assumption of tangential velocity gradient continuity is accurate at the porous interface, even for a high-porosity and high-permeability porous medium as that considered here. A discussion on the topic can be found in the work of Hill & Straughan (2008). The measurement for $Re_h = 100$ (marginally unstable) does not present this velocity gradient discontinuity, presumably due to the mixing caused by the flow undulation.

https://doi.org/10.1017/jfm.2011.422 Published online by Cambridge University Press

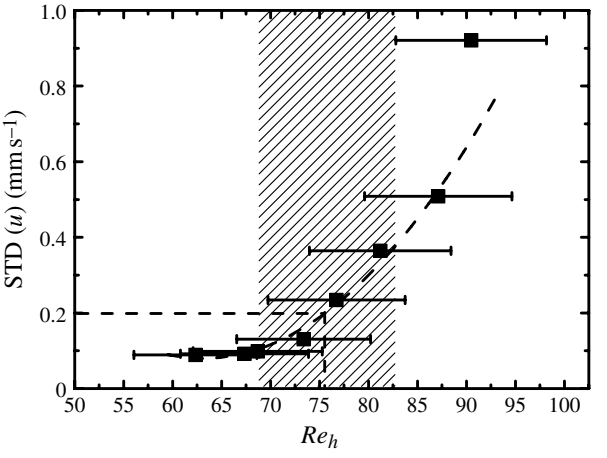


FIGURE 12. Standard deviation of the velocity fluctuations measured at location S_1 and $y = 4$ mm. The error bands results from the propagation of the hot-wire accuracy estimation. The dashed line shows local fitting of measurement with a parabola. It is assumed that critical conditions are reached when the r.m.s. doubles the background level, i.e. it reaches 0.2 mm s^{-1}. The estimated critical Re_h is 76 ± 7.

Figure 11 shows the profile of the root mean square (r.m.s.) of the x component velocity fluctuations u measured for $Re_h = 100$ at position S_1. This profile can be interpreted as the relative amplitude of the instabilities along the y-axis, which should be compared with the x component of the predominant eigenfunction. The curves in figure 11 corresponds to the most unstable mode for $\sigma = 6$ obtained with (2.17) and (2.18) for $Re_h = 100$ and $Re_h = 10\,000$. The latter shows better agreement with the experiments, this can be attributed to end effects of the test section (wave reflections) and/or to nonlinear effects that might result from the amplitude of oscillations. Nevertheless, the correspondence of the peaks at positions -8, 2 and 22 mm is remarkable.

To experimentally determine the critical Reynolds number that triggers instabilities in a rectangular channel flow, Kao & Park (1970) introduced frequency controlled sine-wave perturbations and measured the amplification downstream. However, their technique requires an extremely fine control of the inlet flow, which unfortunately was impossible to achieve in the present case. Another method to estimate the stability margin is to analyse the characteristics of the naturally occurring instabilities, this approach assumes inlet perturbations have a wide spectral content and therefore the most unstable modes will be prevailing downstream. Figure 12 shows the r.m.s. of the velocity signal for different Re_h measured 2 mm just outside the porous region at the axial position S_1. Assuming that the onset of amplification occurs when the r.m.s. doubles the background level at low Re_h, the critical Re_h can be estimated in the range 76 ± 7. This value agrees with the theoretical stability threshold for $\sigma = 6$, i.e. $Re_h = 79$, which is obtained from the contour map of the imaginary part of the eigenvalue of the most unstable mode (figure 13).

The characteristic frequency of the instabilities can be estimated from the power spectral density (figure 14) and the autocorrelation of the streamwise velocity fluctuations u (figure 15) for the case of incipient instability at $Re_h = 100$. The spectrum presents a peak at about $f_p = 1.7$ Hz, which concurs with the first peak of the autocorrelation (0.58 s). To determine the prevailing wavenumber, simultaneous

https://doi.org/10.1017/jfm.2011.422 Published online by Cambridge University Press

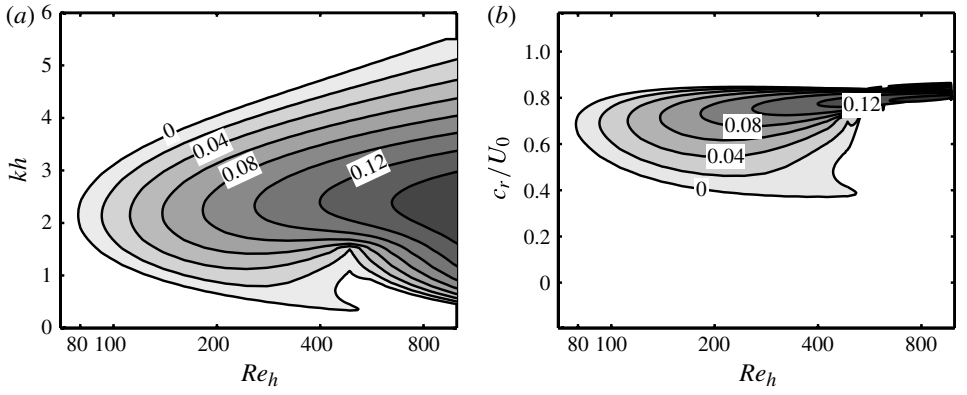


FIGURE 13. Contour maps of the imaginary part of c/U_o in the planes (k, Re_h) and $(c_r/U_o, Re_h)$ for $\sigma = 6$.

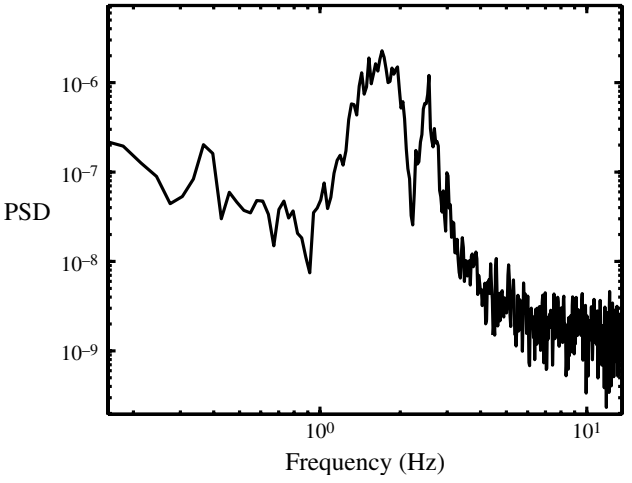


FIGURE 14. Power spectral density of the velocity fluctuations measured at location S_1 and $y = 4$ mm for $Re_h = 100$.

measurements were performed with two probes placed at positions S_1 and S_2, separated 50 mm as shown in figure 9. Both probes were placed at $y = 4$ mm. Figure 15 shows the cross-correlation of both signals, which presents a first peak at 0.43 s. Taking into account that the distance between probes is 50 mm, the wave propagation velocity results $u_p = 0.118$ m s^{-1}. The wavenumber corresponding to the exited mode is then calculated as

$$k = \frac{2\pi f_p}{u_p} \tag{3.5}$$

which gives $k = 2.7 \pm 0.7h^{-1}$. This value is in agreement with the theoretical calculation of the most unstable wavenumber for $\sigma = 6$. As can be observed in figure 13, the unstable wavelength range for $\sigma = 6$ and $Re_h = 100$ is broad and includes $k = 2.7h^{-1}$.

https://doi.org/10.1017/jfm.2011.422 Published online by Cambridge University Press

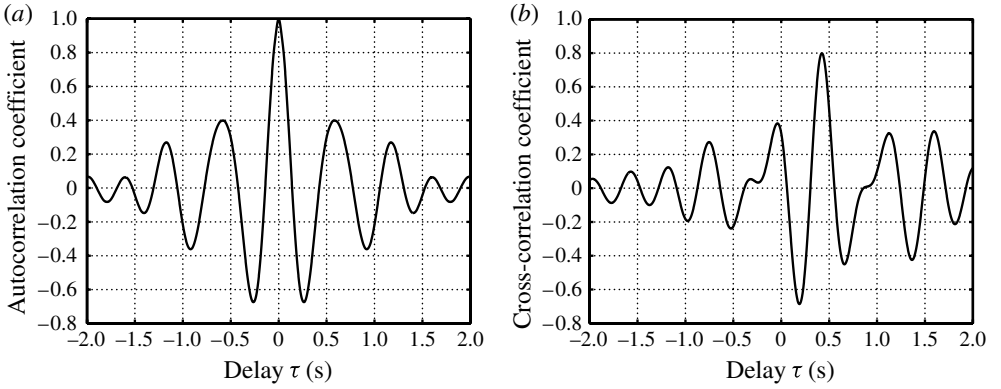


FIGURE 15. Autocorrelation of the velocity fluctuations measured at location S_1, and cross-correlation of the velocity fluctuations measured at locations S_1 and S_2 (in both cases $y = 4$ mm, $Re_h = 100$).

4. Conclusions

A theoretical and experimental study of instabilities in the planar flow between two parallel plates partially obstructed by a porous medium has been presented. An extended Orr–Sommerfeld equation considering a porous medium obeying Darcy's law has been derived and solved numerically to determine the stability margins and the structure of the most unstable velocity perturbation modes. The analysis shows that the porous obstruction generates a mode of instability triggered by the appearance of an inflection point of the velocity profile. For highly permeable media (i.e. $\sigma < 2.1$ when $\beta = 1$) the damping term introduced by the porous obstruction stabilizes the flow, increasing the critical Reynolds number. For lower permeabilities (i.e. $\sigma > 2.1$ when $\beta = 1$) the instability triggered by the inflection point prevails reducing the critical Reynolds number. The most unstable situation corresponds to $\sigma = 6$ with a minimum critical Reynolds number of 79. For a highly resistive porous obstruction the flow becomes more stable. It is worth noting that the two extreme values of σ (0 and ∞) correspond to Poiseuille flows.

The sensitivity to the porous layer depth was also studied. The general trend is that the flow becomes more stable as the porous layer becomes thinner. It has also been found that the transition between instability modes is affected by the depth of the porous layer. Interestingly, for thin porous layers with low permeability, the flow becomes more stable than the corresponding Poiseuille flow.

The theoretical results were compared against an experiment with air flowing through a channel semi-obstructed by a regular array of cylindrical wires. The critical Reynolds number (76 ± 7) was determined by measuring the amplitude of velocity fluctuations at the interface of the porous medium, which agrees with the theoretical result (79). The dominant instability mode was characterized by the cross-section profile of the r.m.s. of the velocity perturbations, which matched reasonable well with the eigenfunction of the most unstable eigenvalue. Also, the wavenumber, $k = (2.7 \pm 0.7)h^{-1}$, determined by correlating the velocity measurements in two sequential locations along the channel, compares well with the theoretical value (2.1).

The present conclusions should be used carefully when addressing unbounded flows. Simply applying a very large value of σ may not be an appropriate approximation, as the flow stability does depend on the velocity profile. The study of this kind of

https://doi.org/10.1017/jfm.2011.422 Published online by Cambridge University Press

problem can be the object of further research, for which it is hoped that the results presented in this work would be helpful.

Acknowledgements

The authors would like to thank D. Osorio for his assistance in the electronics of the experiment and F. Teruel of the Computational Mechanics group of Centro Atomico Bariloche for his useful discussions.

REFERENCES

BEAVERS, G. & JOSEPH, D. D. 1967 Boundary conditions at a naturally permeable wall. *J. Fluid Mech.* **30**, 197–207.

BOUSMAR, D., RIVIÈRE, P. N., PAQUIER, A., MOREL, R. & ZECH, Y. 2005 Upstream discharge distribution in compound-channel flumes. *J. Hydraul. Engng* **131**, 408–412.

BREUGEM, W. P., BOERSMA, B. J. & UITTENBOGAARD, R. E. 2006 The influence of wall permeability on turbulent channel flow. *J. Fluid Mech.* **562**, 35–72.

BRUUN, H. H. 1995 *Hot Wire Anemometry: Principles and Signal Analysis*. Oxford University.

CHEW, Y. T., KHOO, B. C. & LI, G. L. 1998 An investigation of wall effects on hot-wire measurements using a bent sublayer probe. *Meas. Sci. Technol.* **9**, 67–85.

FINNIGAN, J. 2000 Turbulence in plant canopies. *Annu. Rev. Fluid Mech.* **32**, 519–571.

GAYEV, Y. A. & HUNT, J. C. R. 2007 *Flow and Transport Processes with Complex Obstructions*, *Series II: Mathematics, Physics and Chemistry*, 236. Springer.

GHISALBERTI, M. 2009 Obstructed shear flows: similarities across systems and scales. *J. Fluid Mech.* **641**, 51–61.

HILL, A. A. & STRAUGHAN, B. 2008 Poiseuille flow in a fluid overlying a porous medium. *J. Fluid Mech.* **603**, 137–149.

KAO, T. W. & PARK, C. 1970 Experimental investigations of the stability of channel flows. Part 1. Flow of a single liquid in a rectangular channel. *J. Fluid Mech.* **43**, 145–164.

LARSON, R. E. & HIGDON, J. J. L. 1986 Microscopic flow near the surface of two-dimensional porous media. Part l. Axial flow. *J . Fluid Mech.* **166**, 444–472.

LARSON, R. E. & HIGDON, J. L. 1987 Microscopic flow near the surface of two-dimensional porous media. Part 2. Transverse flow. *J. Fluid Mech.* **178**, 119–136.

LEXMOND, A. S., MUDDE, R. F. & VAN DER HAGEN, T. H. 2005 Visualisation of the vortex street and characterisation of the cross flow in the gap between two sub-channels, *Eleventh Int. Topical Meeting on Nuclear Reactor Thermal-Hydraulics (NURETH-11)*, Avignon, France, 2–6 October, Paper 122.

LÓPEZ, F. & GARCÍA, M. H. 2001 Mean flow and turbulence structure of open-channel flow through non-emergent vegetation. *J. Hydraul. Engng* **127**, 392–402.

MATHIEU, J. & SCOTT, J. 2000 *An Introduction to Turbulent Flow*, p. 17. Cambridge University Press.

MERZARI, E., WANG, S., NINOKATA, H. & THEOFILIS, V. 2008 Biglobal linear stability analysis for the flow in eccentric annular channels and a related geometry. *Phys. Fluids* **20**, 114104.

MEYER, L. 2010 From discovery to recognition of periodic large scale vortices in rod bundles as source of natural mixing between subchannels – A review. *Nucl. Engng Des.* **240**, 1575–1588.

MEYER, L. & REHME, K. 1995 Periodic vortices in flow through channels with longitudinal slots or fins. *Proceedings of the Tenth Symposium on Turbulent Shear Flows*, University Park, PA, 14–16 August, vol. 2, S.P2/55–P2/60.

POGGI, D. & KATUL, G. G. 2008 Micro and macro dispersive fluxes in canopy flows. *Acta Geophys.* **56**, 778–800.

RAUPACH, M. R., FINNIGAN, J. J. & BRUNET, Y. 1996 Coherent eddies and turbulence in vegetation canopies: the mixing-layer analogy. *Boundary-Layer Meteorol.* **78**, 351–382.

https://doi.org/10.1017/jfm.2011.422 Published online by Cambridge University Press

SCHLICHTING, H. & GERSTEN, K. 2000 *Boundary-Layer Theory*. McGraw Hill, 1979.

SOCOLOFSKY, S. A. & JIRKA, G. H. 2004 Large-scale flow structures and stability in shallow flows. *J. Environ. Engng Sci.* **3**, 451–462.

WEIDEMAN, J. A. C. & REDDY, S. C. 2000 A MATLAB differentiation matrix suite. *ACM Trans. Math. Softw.* **26**, 465–519.

WHITE, B. L. & NEPF, H. M. 2007 Shear instability and coherent structures in shallow flow adjacent to a porous layer. *J. Fluid Mech.* **593**, 1–32.

YUE, Z. & MALMSTROM, T. G. 1998 A simple method for low-speed hot-wire anemometer calibration. *Meas. Sci. Technol.* **9**, 1506.

https://doi.org/10.1017/jfm.2011.422 Published online by Cambridge University Press